Available online at www.sciencedirect.com
SCIENCE DIRECT®
Journal of Solid State Chemistry 177 (2004) 4687–4694
JOURNAL OF SOLID STATE CHEMISTRY
www.elsevier.com/locate/jssc

Preparation, structure and photoluminescence properties of Eu^{2+} and Ce^{3+}-doped $SrYSi_4N_7$

Y.Q. Li*, C.M. Fang, G. de With, H.T. Hintzen*

Laboratory of Solid State and Materials Chemistry, Eindhoven University of Technology, P.O. Box 513, 5600 MB Eindhoven, The Netherlands

Received 25 May 2003; received in revised form 24 July 2004; accepted 26 July 2004

Abstract

Undoped and Eu^{2+} or Ce^{3+}-doped $SrYSi_4N_7$ were synthesized by solid-state reaction method at 1400–1660 °C under nitrogen/hydrogen atmosphere. The crystal structure was refined from the X-ray powder diffraction data by the Rietveld method. $SrYSi_4N_7$ and $EuYSi_4N_7$, being isotypic with the family of compounds $MYbSi_4N_7$ (M = Sr, Eu, Ba) and $BaYSi_4N_7$, crystallize with the hexagonal symmetry: space group $P6_3mc$ (No. 186), $Z=2$, $a=6.0160$ (1) Å, $c=9.7894$ (1) Å, $V=306.83(3)$ Å^3; and $a=6.0123$ (1) Å, $c=9.7869$ (1) Å, $V=306.37(1)$ Å^3, respectively. Photoluminescence properties have been studied for $Sr_{1-x}Eu_xYSi_4N_7$ ($x=0$–1) and $SrY_{1-x}Ce_xSi_4N_7$ ($x=0$–0.03) at room temperature. Eu^{2+}-doped $SrYSi_4N_7$ shows a broad yellow emission band peaking around 548–570 nm, while Ce^{3+}-doped $SrYSi_4N_7$ exhibits a blue emission band with a maximum at about 450 nm. $SrYSi_4N_7$:Eu^{2+} can be very well excited by 390 nm radiation, which makes this material attractive as conversion phosphor for LED lighting applications.

Keywords: Crystal structure; Rietveld refinement; Europium; Cerium; Luminescence; Phophor; Rare-earth silicon nitride

1. Introduction

Rare-earth ions have an important role in silicon nitride, Sialon and related nitride materials. Rare-earth oxides are often used as sintering aids not only lowering the sintering temperature but also improving high temperature and creep properties [1,2]. On the other hand, rare-earth doped phosphors are also used in modern fluorescent lamps, displays and X-ray intensifying/scintillation screens, such as $LaPO_4$:Ce,Tb, Y_2O_3:Eu, Y_2O_2S:Eu and Y_2SiO_5:Ce, as well as $YTaO_4$:Nb [3,4]. In recent years, it has been shown that rare earth ion-doped silicon/aluminum nitrides and oxynitrides might be promising phosphor materials [5–11].

In recent years several new quaternary rare earth containing silicon nitride compounds like $MYbSi_4N_7$ (M = Sr, Ba, Eu) were prepared and characterized [12,13]. The crystal structure of these compounds is different from the conventional metal-silicon nitride compounds. Although the framework in $MYbSi_4N_7$ is also built up by the basic building block of corner-sharing SiN_4 tetrahedra, no NSi_3 ($N^{[3]}$) units are present. Instead, an unusual $N^{[4]}$ atom which is coordinated by four silicon atoms is found, besides $N^{[2]}$ ions [12–14]. The bond lengths to the $N^{[4]}$ atoms are significantly larger than those to the twofold coordinated $N^{[2]}$ atoms. Recently, we successfully prepared the pure $BaYSi_4N_7$ compound which is isotypic with $MYbSi_4N_7$ and determined the optical properties of the undoped [15] and rare-earth doped [16] materials.

Based on the fact that an amount of Y^{3+} and Yb^{3+}, Sr^{2+} and Eu^{2+} containing compounds are isostructural in oxynitrides and nitrides, like $LnSi_3O_3N_4$ (Ln = Y, Yb), $MYbSi_4N_7$ (M = Sr, Eu) and MSi_2N_5 (M = Sr, Eu), it is interesting to synthesise the $SrYSi_4N_7$ and

*Corresponding author. Faculteit Scheikundige Technologie, Technische Universiteit Eindhoven, Vastestof-en Materiaalchemie (SVM), Postbus Box 513 (Helix Building), NL-5600 MB Eindhoven, The Netherlands. Tel.: +31-40-2473059; Fax: +31-40-2445619.

E-mail addresses: y.q.li@tue.nl (Y.Q. Li), h.t.hintzen@tue.nl (H.T. Hintzen).

0022-4596/$ - see front matter © 2004 Elsevier Inc. All rights reserved.
doi:10.1016/j.jssc.2004.07.054

$EuYSi_4N_7$ compounds. If the two compounds really exist with the same crystal structure, it is expected that complete solid solutions are formed and the optical properties can be tuned by varying the Eu^{2+} concentration. Apart from the Sr^{2+} site, also the Y^{3+} site in $SrYSi_4N_7$ is available for trivalent activator ions like Ce^{3+}, and it is of interest to compare the results for this material with our previous results obtained for $BaYSi_4N_7$:Ce [16].

In the present study, we report the preparation of $MYSi_4N_7$ (M=Sr, Eu) compounds by solid-state method and the determination of their crystal structure by Rietveld refinement of X-ray diffraction measurements. In addition, a series of varying compositions $Sr_{1-x}Eu_xYSi_4N_7$ and $SrY_{1-x}Ce_xSi_4N_7$ are synthesized and we report on the luminescence properties of Eu^{2+} or Ce^{3+}-doped $SrYSi_4N_7$.

2. Experimental

Powder samples of $Sr_{1-x}Eu_xYSi_4N_7$ ($0 \leqslant x \leqslant 1$) and $SrY_{1-x}Ce_xSi_4N_7$ ($0 \leqslant x \leqslant 0.05$) compounds were prepared by solid-state reaction from stoichiometric quantities of high purity grade Si_3N_4 (two types, viz. (1) Cerac S-1177, measured β content: 91%, N content: 38.35%; O content: ~0.7%, with purity 99.5%; (2) Permascand Grade P95H, measured α content: 91%, N content: 38.08%; O content: ~1.5%, with purity 99%), Y (Csre, 99.9%, powder), Sr (Aldrich, 99%, pieces), Ce (Alfa, 99%, pieces) and Eu (Csre, 99.9%, pieces). SrN_x (x~0.65) and Eu-nitride (approximately EuN) were presynthesized by a nitriding reaction of Sr and Eu metals under nitrogen atmosphere at 800–850 °C, and then grinding them into fine powders. The starting mixtures were thoroughly mixed and ground with an agate mortar and pestle. All manipulations were carried out in a protecting atmosphere in a glove box filled with dry nitrogen because of the great air sensitivity of most of the raw materials. Subsequently the well-mixed starting powders were placed in a molybdenum crucible and fired at 1400 and 1660 °C for 12 and 16 h, respectively, under a flowing gas mixture 5%H_2–95%N_2 in horizontal tube furnaces with an intermediate grinding between the firing steps.

Powder X-ray diffraction (XRD) data were collected on a Rigaku D/Max-γB diffractometer with Bragg–Brentano geometry (flat graphite monochromator, scintillation counter) using Cu$K\alpha$ radiation operating at 40 kV, 30 mA at room temperature. The lattice parameters were determined in the 2θ range of 10–90° using step scan mode (step size 0.01°, counting time per step 10 s) using Si powder as an internal standard reference. For the Rietveld analysis, the powder diffraction data were recorded in the 2θ range of 10–120° using step scan mode (step size 0.01°, counting time per step 20 s) on finely ground samples. A 1° divergence and scatter slit together with a 0.3° receiving slit were employed for the measurements. Rietveld refinement [17] was performed using the program GSAS [18,19]. The scaling factor, the zero point, the background and the lattice parameters were refined initially. A pseudo-Voigt function was chosen to fit the profile. The preferential orientation was also refined with the March–Dollase function.

The photoluminescence spectra were recorded at room temperature on powder samples by a Perkin-Elmer LS-50B luminescence spectrometer with Monk–Gillieson type monochromators and a 20 kW Xenon discharge lamp as excitation source. The spectra were obtained in the range of 200–900 nm with a scanning speed of 100 nm/min. Diffuse reflectance spectra were recorded in the range of 230–700 nm with $BaSO_4$ white powder and black felt as the reference materials. Excitation spectra were automatically corrected for the lamp intensity by a second photomultiplier. All the emission spectra were corrected by taking into account the combined effect of the spectral response of the detector and the transmission of the monochromator using the measured spectra of a calibrated W-lamp as the light source.

3. Results and discussion

3.1. Preparation

In the introductory investigation of the synthesis processes, we used α-Si_3N_4 (O content: ~1.5%) powder as the raw material. However, a large amount of secondary phases like, $Sr_2Si_5N_8$ or $Eu_2Si_5N_8$ and unidentified phases was present in the final product, even when the sample was fired at high temperatures for a long time. After changing the starting Si_3N_4 powder from α to the normally less reactive β-Si_3N_4 (O content: ~0.7%), high phase purity compounds of $SrYSi_4N_7$ and $EuYSi_4N_7$ could be obtained. X-ray powder diffraction analysis showed that a small amount (<9%) of YSi_3N_5 [20] is present in the final samples. Apart from YSi_3N_5, still some peaks due to traces of $Sr_2Si_5N_8$ or $Eu_2Si_5N_8$ are also detected in the $SrYSi_4N_7$ and $EuYSi_4N_7$ samples as well as their solid solutions. It is well known that α-Si_3N_4 has a higher oxygen content (O content: 1.2–2.5%) than β-Si_3N_4 powder (O content: <1%) [21]. In addition, the Y powder also contains a small amount of oxygen impurity. On the contrary for $BaYSi_4N_7$ single phase material can be obtained easily with both α- and β-Si_3N_4 [15,16]. Our experiments have shown that with the cation size decreasing going from Ba to Ca the preparation of $MYSi_4N_7$ becomes more difficult, $CaYSi_4N_7$ could even not be obtained at all. Possibly oxygen can be incorporated by replacing nitrogen when

the divalent ion is sufficiently small to be incorporated on the Y-site for charge compensation, ultimately resulting in structure breakdown. The sensitivity to oxygen was confirmed by our experiments showing that the sample became purer by firing several times at high temperatures for a long time using α-Si_3N_4 in an atmosphere of mixed N_2–H_2 (10%) with the purpose to remove oxygen from its lattice. It has been proved that long term heat treatment under reducing atmosphere is an effective way to eliminate the lattice oxygen from AlN ceramics [22]. Based on the same considerations, only β-Si_3N_4 starting powder with low oxygen content was used as raw material in the further investigations.

3.2. Structure determination

The X-ray powder diffraction patterns of $SrYSi_4N_7$ and $EuYSi_4N_7$ are found to be similar to those of $MYbSi_4N_7$ (M = Sr, Ba, Eu) [12–14] and $BaYSi_4N_7$ [16]. Therefore, the structure of $SrYbSi_4N_7$ (space group: $P6_3mc$) was employed as the starting model for the Rietveld refinement of the structures of $SrYSi_4N_7$ and $EuYSi_4N_7$.

Since the prepared samples contained a small amount of impurity phases (YSi_3N_5, $Sr_2Si_5N_8$ or $Eu_2Si_5N_8$), some parts of the data were excluded for the refinement. All atomic positions and equivalent isotropic displacement parameters were refined converging to the residual factors R_{wp} = 9.33%, R_p = 5.96%; and R_{wp} = 11.38%, R_p = 8.33% for $SrYSi_4N_7$ and $EuYSi_4N_7$, respectively. The resulting crystallographic data are summarized in Table 1. The atomic coordinates and equivalent isotropic displacement parameters are given in Table 2. A list of selected bond distances and angles is gathered in Table 3. The final calculated and observed diffraction patterns are presented in Fig. 1 ($SrYSi_4N_7$) and Fig. 2 ($EuYSi_4N_7$), respectively.

The structure of $MYSi_4N_7$ being isostructural with $MYbSi_4N_7$ consists of SiN_4 tetrahedra which share corners, in this way forming a three-dimensional network structure with large channels along [100] and [010] formed by Si_6N_6 rings. Both Sr^{2+} (or Eu^{2+}) and Y^{3+} ions occupy a site in the above mentioned channels. The Sr^{2+} (or Eu^{2+}) ion is coordinated by twelve nitrogen atoms (SrN_{12} or EuN_{12}) and the Y^{3+} ion is coordinated by six nitrogen atoms (YN_6). In the network one N atom (N3) connects four Si atoms ($N^{[4]}$) and the other N atoms (N1 and N2) connect two Si atoms ($N^{[2]}$) without the presence of $N^{[3]}$ atoms as is usual the case in metal silicon nitrides [12–14]. The building tetrahedral units of $[N(SiN_3)_4]$ are linked by sharing $N^{[2]}$ atoms extending along the a- and b-axis (Fig. 3). The mean Si–N distance in $EuYSi_4N_7$ is about 0.03 Å smaller as compared with $SrYSi_4N_7$. The Si2–N1 and Si2–N2 distances almost reach the minimal value of the range typical for metal silicon nitride compounds [23,24] which indicates that the Si–N network in $EuYSi_4N_7$ is distorted as compared with that of $SrYSi_4N_7$, as shown in Fig. 4. It is worth noting that such significantly different interatomic distances of Si–N in $SrYSi_4N_7$ and $EuYSi_4N_7$ may be responsible for the formation of the small amounts of the impurity phases observed in the solid solution samples (see below), especially at Eu-rich side. Some individual atomic displacement parameters show a little bit difference in $SrYSi_4N_7$ and $EuYSi_4N_7$ (Table 2). Because these parameters represent the combined total of several effects in addition to displacements caused by thermal motion, we will not give a further discussion.

Accurate cell parameters of $Sr_{1-x}Eu_xYSi_4N_7$ ($0 \leqslant x \leqslant 1$) compounds were determined by the Rietveld method. Fig. 5(a) shows the variation of the a, c

Table 1
Crystallographic data for $SrYSi_4N_7$ and $EuYSi_4N_7$

Formula	$SrYSi_4N_7$	$EuYSi_4N_7$
Formula weight	486.92	451.26
Crystal system	Hexagonal	Hexagonal
Space group	$P6_3mc$ (no. 186)	$P6_3mc$ (no. 186)
Cell parameters (Å)	a = 6.0160(1)	a = 6.0123 (1)
	c = 9.7894(1)	c = 9.7869 (2)
Cell volume (Å^3)	306.83 (1)	306.37 (1)
Z	2	2
Density, calculated (g/cm^3)	4.188	4.891
T (K)	298	298
2θ (deg) range	10–120	10–120
Scan conditions	Step size 0.01, 20 s/step	
R-factors		
wR_p	0.0933	0.1138
R_p	0.0596	0.0833
R_F^2	0.0484	0.0991
χ^2	8.04	8.96

Table 2
Atomic coordinates and isotropic displacement parameters of $SrYSi_4N_7$ and $EuYSi_4N_7$

Atom	Wyckoff	Symm.	x	y	z	U_{iso} (Å)
Y	2*b*	3*m*	1/3	2/3	0.4552(4)	0.0032
Sr	2*b*	3*m*	1/3	2/3	0.08448(35)	0.0065
Si1	2*a*	3*m*	0	0	0.5297(5)	0.0031
Si2	6*c*	*m*	0.82655(18)	0.6531(4)	0.26008(27)	0.0034
N1	6*c*	*m*	0.5138(4)	0.4862(4)	0.3125(4)	0.0013
N2	6*c*	*m*	0.1512(5)	0.3025(9)	0.5855(5)	0.0065
N3	2*a*	3 m	0	0	0.3292(8)	0.0028
Y	2*b*	3*m*	1/3	2/3	0.4590(6)	0.0029
Eu	2*b*	3*m*	1/3	2/3	0.0896(6)	0.0100
Si1	2*a*	3*m*	0	0	0.5156(12)	0.0040
Si2	6*c*	*m*	0.8271(4)	0.6543(8)	0.2685(7)	0.0026
N1	6*c*	*m*	0.5177(11)	0.4823(11)	0.2986(10)	0.0052
N2	6*c*	*m*	0.1479(8)	0.2960(16)	0.6004(12)	0.0033
N3	2*a*	3*m*	0	0	0.3250(17)	0.0108

Table 3
Selected bond distances (Å) and angles (deg)

$SrYSi_4N_7$				$EuYSi_4N_7$			
Sr–N1	2.918(5) (× 3)	N1–Sr–N1	67.82(18) (× 3)	Eu–N1	2.806(12) (× 3)	N1–Eu–N1	72.7(4) (× 3)
Sr–N1	3.103(5) (× 3)	Si1–N2–Si2	116.8(4)	Eu–N1	3.243(13) (× 3)	Si1–N2–Si2	127.2(7)
Sr–N2	3.013(1) (× 3)	Si1–N3–Si2	110.5 (3) (× 3)	Eu–N2	3.015(1) (× 3)	Si1–N3–Si2	107.1(6) (× 3)
Sr–N2	3.012(1) (× 3)	Si2–N3–Si2	108.4(3) (× 3)	Eu–N2	3.014(1) (× 3)	Si2–N3–Si2	111.8(5) (× 3)
Y–N1	2.342(3) (× 3)	N1–Y–N1	88.06(13) (× 3)	Y–N1	2.481(11) (× 3)	N1–Y–N1	84.2(4) (× 3)
Y–N2	2.286(5) (× 3)	N1–Y–N2	89.99(13) (× 3)	Y–N2	2.375(11) (× 3)	N1–Y–N2	176.4(5) (× 3)
Si1–N2	1.668(5) (× 3)	N1–Y–N2	89.98(13) (× 3)	Si1–N2	1.750(10) (× 3)	N1–Y–N2	93.12(28)(× 3)
Si1–N3	1.962(9)	N1–Y–N2	177.29(18) (× 3)	Si1–N3	1.866(15)	N1–Y–N2	93.11(28)(× 3)
Si2–N1	1.710(1)) (× 2)	N2–Y–N2	91.89 (19) (× 3)	Si2–N1	1.641(4) (× 2)	N2–Y–N2	89.5(4) (× 3)
Si2–N2	1.724(5)	N2–Si1–N2	109.80(27) (× 3)	Si2–N2	1.665(13)	N2-Si1–N2	99.4(6) (× 3)
Si2–N3	1.930(4)	N2–Si1–N3	109.14(27) (× 3)	Si2–N3	1.883(7)	N2–Si1–N3	118.3(5) (× 3)
		N1–Si2–N3	111.78(22) (× 2)			N1–Si2–N3	118.0(5) (× 2)
		N1–Si2–N1	107.62(34)			N1–Si2–N1	109.9(9)
		N1–Si2–N2	111.43(19) (× 2)			N1–Si2–N2	105.2(5) (× 2)

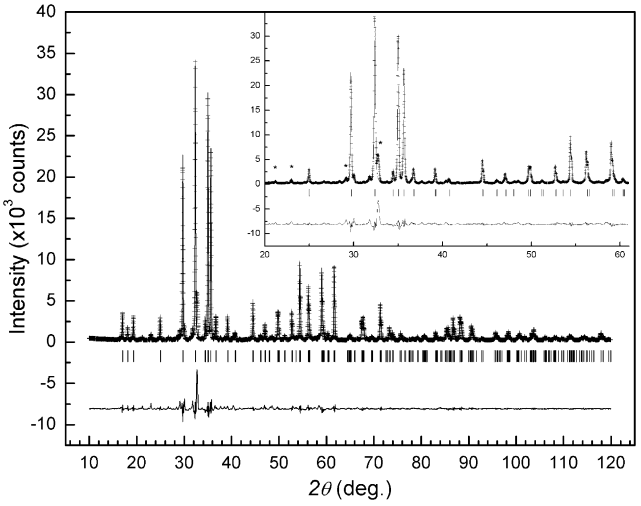

Fig. 1. The Rietveld refinement pattern for $SrYSi_4N_7$ using X-ray powder diffraction data. Plus (+) marks represent the observed intensities, and the solid line the calculated patterns. A difference (obs.–calc.) plot is shown at the bottom. The tick marks above the difference data indicate the positions of Bragg reflections for $SrYSi_4N_7$. The asterisk (*) in inset indicates the impurity peaks.

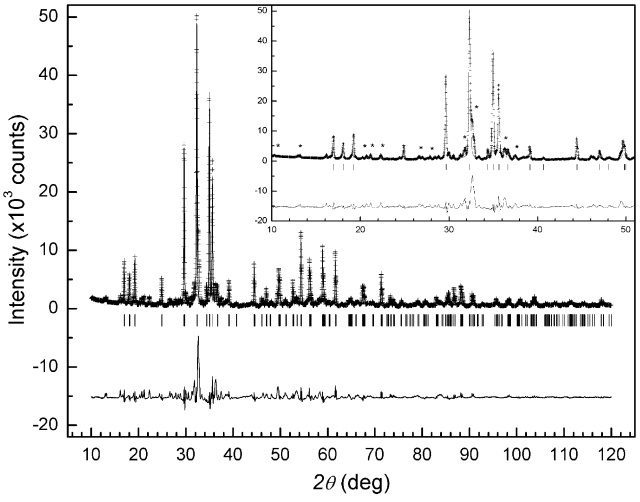

Fig. 2. The Rietveld refinement pattern for $EuYSi_4N_7$ using X-ray powder diffraction data. Plus (+) marks represent the observed intensities, and the solid line the calculated patterns. A difference (obs.–calc.) plot is shown at the bottom. The tick marks above the difference data indicate the positions of Bragg reflections for $EuYSi_4N_7$. The asterisk (*) in inset indicates the impurity peaks.

parameters and unit cell volume (V) versus x. The a and V parameters decrease with increasing Eu concentration going from 6.0160 (1) Å, 306.83 (3) Å^3 to 6.0138 (1) Å, 306.46 (1) Å^3 for undoped and Eu-doped ($x=0.3$) samples. The decrease is in agreement with the fact that the ionic radius of the Eu^{2+} ion is slightly smaller than that of the Sr^{2+} ion [25]. The c/a ratio of $Sr_{1-x}Eu_xYSi_4N_7$ is almost constant for all x values (~1.627). Therefore, it can be concluded that the overall structural shrinkage of $Sr_{1-x}Eu_xYSi_4N_7$ lattice is isotropic. When $x>0.3$ the lattice parameters still slightly decrease but a significant amount of secondary phases, like YSi_3N_5 and $(Sr, Eu)_2Si_5N_8$, is present in the samples. Therefore, the lattice parameters in the x range between 0.3 and 0.9 are not given.

The lattice parameters of $SrY_{1-x}Ce_xSi_4N_7$ ($0\leqslant x\leqslant 0.05$) compounds are shown in Fig. 5(b). As expected, with increasing Ce concentration the lattice parameters show a slight increase because of Ce^{3+} being larger than the Y^{3+} ion [25]. A very limited solubility of Ce in $SrYSi_4N_7$ is found around $x=0.03$.

3.3. Reflection spectra of the undoped and doped $SrYSi_4N_7$ compounds

The diffuse reflectance spectra of undoped, Eu-doped and Ce-doped $SrYSi_4N_7$ samples are shown in Fig. 6. The reflection spectrum of undoped $SrYSi_4N_7$ shows an absorption edge at about 350–375 nm (corresponding with the valence to conduction band transitions of the

host lattice) indicating that the band gap of the $SrYSi_4N_7$ compound is about 3.3–3.5 eV, in fair agreement with our results (2.9 eV) estimated by the first-principles calculations [15].

The incorporation of Eu^{2+} ions into the $SrYSi_4N_7$ lattice results in broad absorption bands in the range of 300–450 nm. With increasing Eu concentration the onset of the absorption band gradually extends to longer wavelengths into the visible part of the spectrum (Fig. 6a). Correspondingly, the daylight color of the

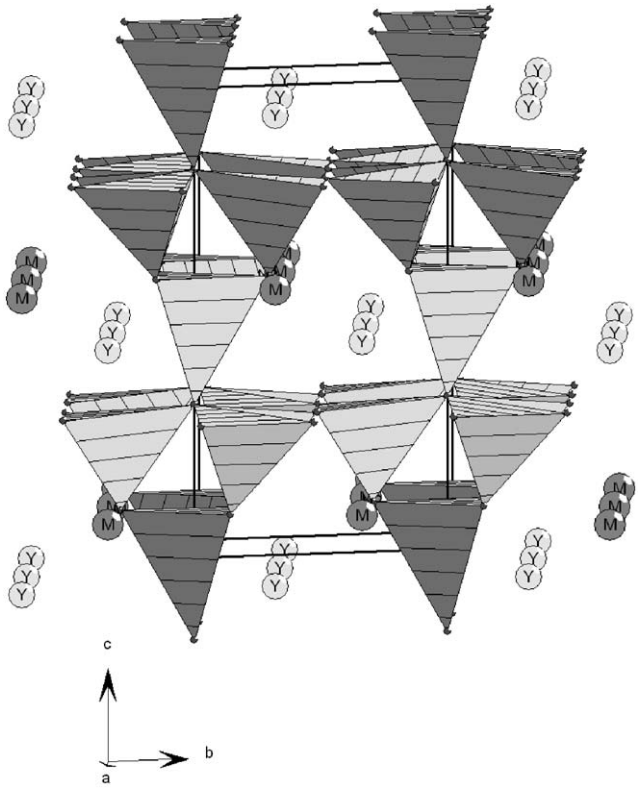

Fig. 3. Schematic illustration of crystal structure of $MYSi_4N_7$ (M = Sr, Eu) along [100].

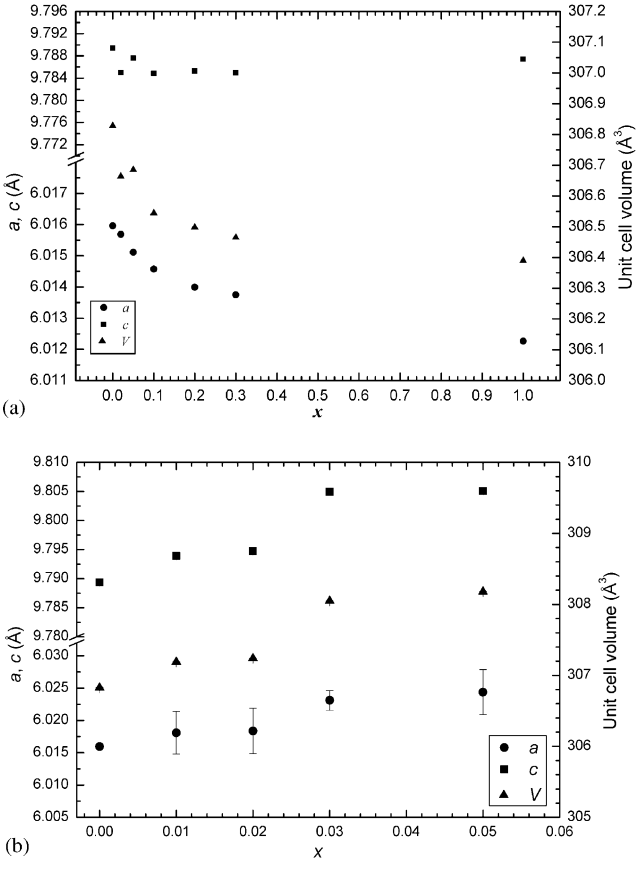

Fig. 5. The lattice parameters as a function of x in (a) $Sr_{1-x}Eu_xYSi_4N_7$ and (b) $SrY_{1-x}Ce_xSi_4N_7$.

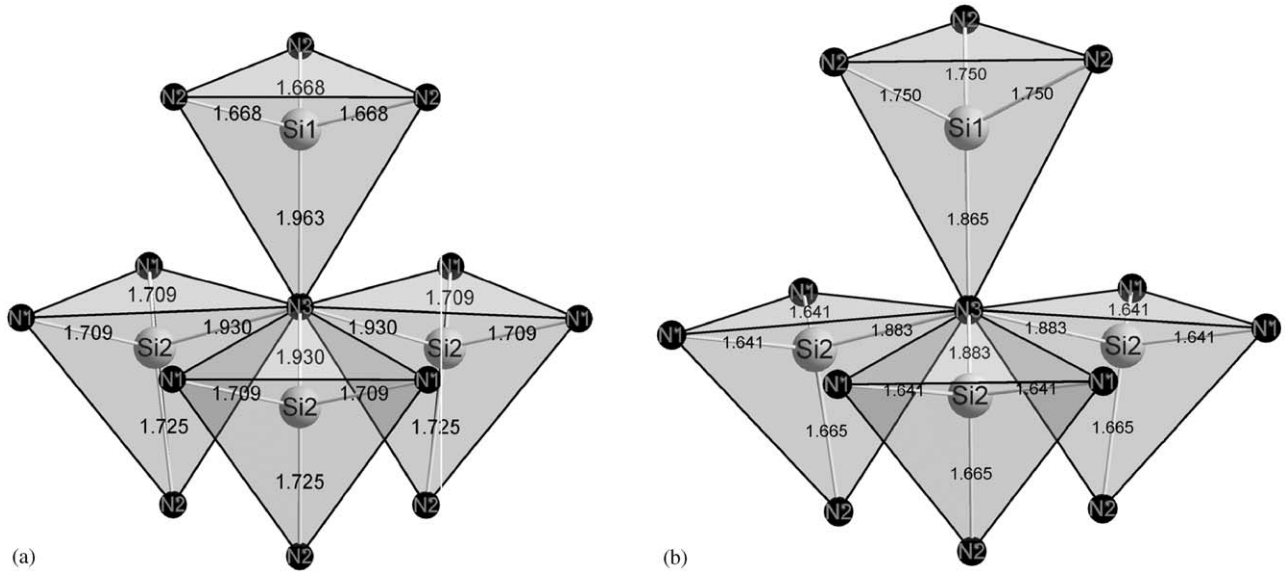

Fig. 4. The $[N(SiN_3)_4]$ building groups in (a) $SrYSi_4N_7$ and (b) $EuYSi_4N_7$.

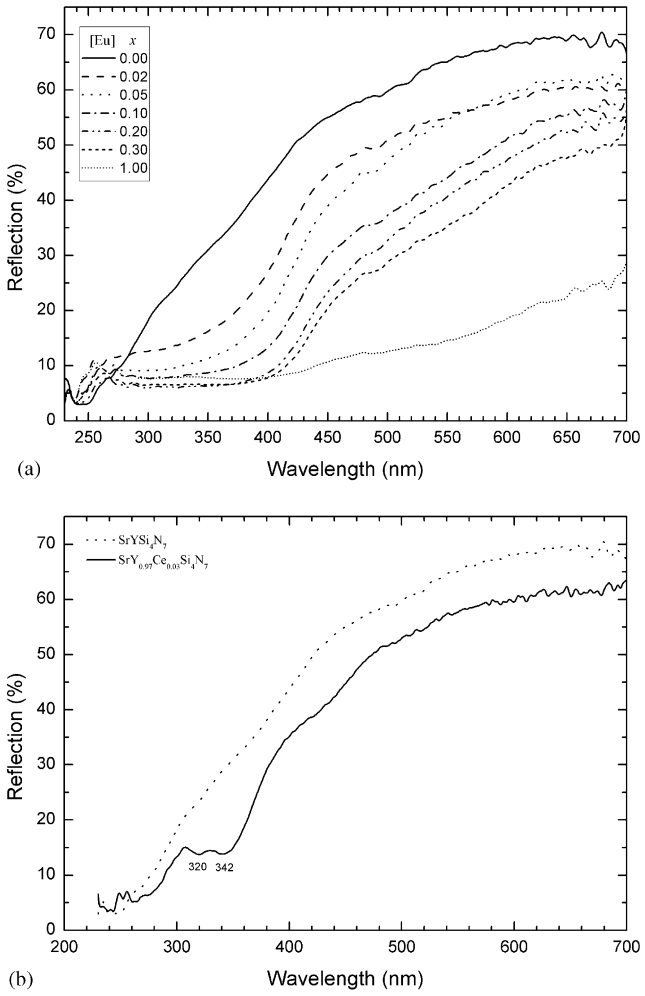

Fig. 6. Reflection spectra of (a) $Sr_{1-x}Eu_xYSi_4N_7$, and (b) $SrY_{1-x}Ce_xSi_4N_7$ ($x=0.03$). For comparison, $EuYSi_4N_7$ is also presented in (a).

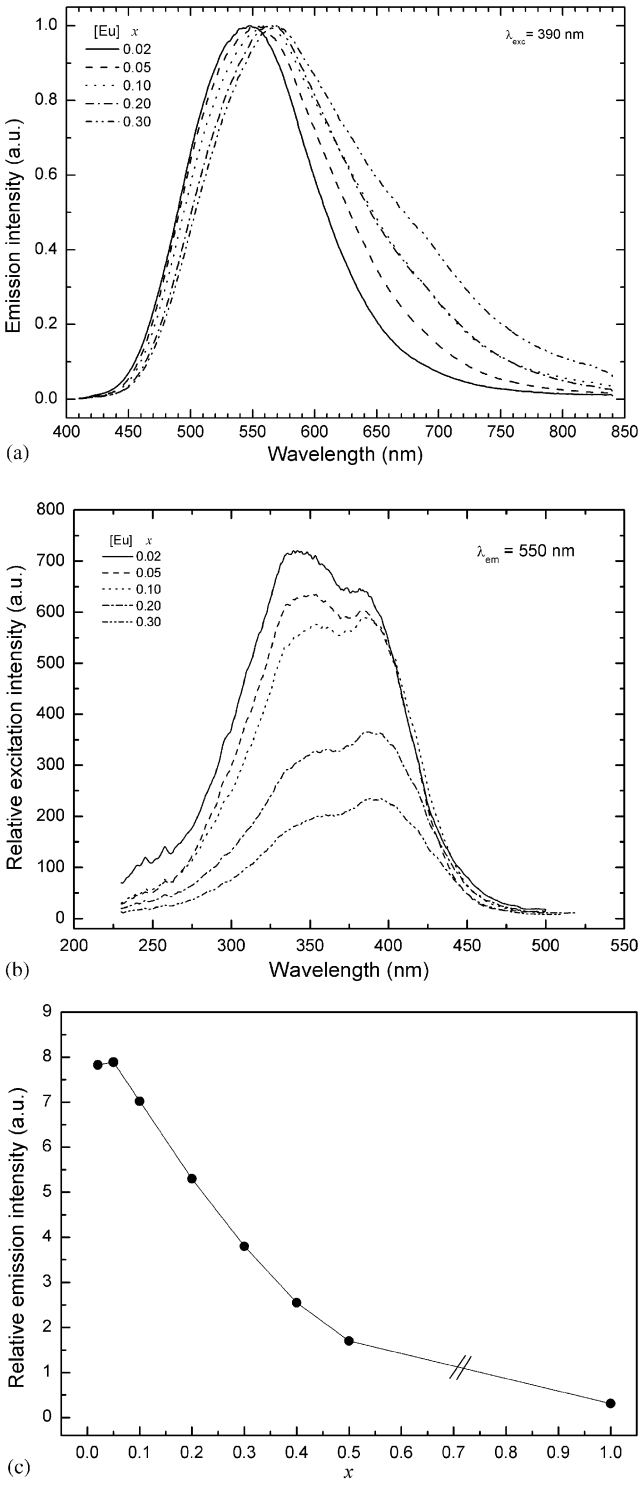

Fig. 7. (a) Emission spectra ($\lambda_{exc}=390$ nm), (b) excitation spectra ($\lambda_{em}=550$ nm) and (c) Eu^{2+} concentration dependence of emission intensity for $Sr_{1-x}Eu_xYSi_4N_7$ ($0<x\leqslant 1$).

samples changes from yellow green to orange and dark red for the Eu-rich samples.

The Ce^{3+}-doped $SrYSi_4N_7$ displays a pronounced doublet absorption band in the region of 310–350 nm (Fig. 6b), similar to $BaYSi_4N_7$:Ce^{3+} [16]. The doublet band peaking at about 320 and 342 nm correspond to splitting of the $4f\rightarrow 5d$ excitation band (see next section). These absorption bands thereby demonstrate a good ability to be stimulated in this region by UV.

3.4. Luminescence properties

3.4.1. $SrYSi_4N_7$:Eu^{2+}

The emission spectra of $SrYSi_4N_7$:Eu^{2+} at room temperature show a broad band at about 550 nm (Fig. 7a). This emission band corresponds to the $4f^6 5d\rightarrow 4f^7$ transition of Eu^{2+}. Obviously, the emission bands of samples doped with a low Eu concentration appear to be symmetric indicating that only a single Eu site is present in the $SrYSi_4N_7$ lattice. With increasing Eu content the emission band exhibits a red-shift from 548 to 570 nm. In addition, an emission shoulder around 660–680 nm in the spectra becomes evident. Because $SrYSi_4N_7$ and $EuYSi_4N_7$ are isotypic and only one crystallographic site is available for the divalent cation, this shoulder (second

band) probably is originating from the second phase (Sr, Eu)$_2$Si$_5$N$_8$ as described before.

The excitation spectra of SrYSi$_4$N$_7$:Eu^{2+} (Fig. 7b) show broad bands peaking at about 340 and 390 nm, matching the absorption range as observed in the reflection spectra (Fig. 6a). Normally, when the Eu^{2+} ion occupies a lattice site with C_{3v} symmetry a splitting into three 5*d* bands is expected in the excitation spectra. Due to serious overlap, especially for high Eu concentrations, only two distinct 5*d* bands can be observed in the excitation spectra. SrYSi$_4$N$_7$:Eu can thus be well excited with a GaN-based LED, which makes this material promising for LED lighting applications. The relative intensity of excitation systematically decreases with increasing Eu concentration. The emission intensity monitored at an excitation wavelength of 390 nm shows a maximum at around $x=0.05$. When $x>0.05$ the emission intensity decreases dramatically (Fig. 7c).

The Stokes shift, roughly estimated from the maxima in the excitation and emission spectra, increases from about 7900 cm^{-1} for lower Eu contents to 8300 cm^{-1} for higher Eu concentrations (Fig. 8). The Stokes shift becomes larger as expected for total lattice contraction arising from the substitution of Eu^{2+} for Sr^{2+} ions, while the mean Eu–N distance has a negligible influence (Fig. 8, Table 3). The mean bond length, i.e. Eu$_{Sr}$–N,

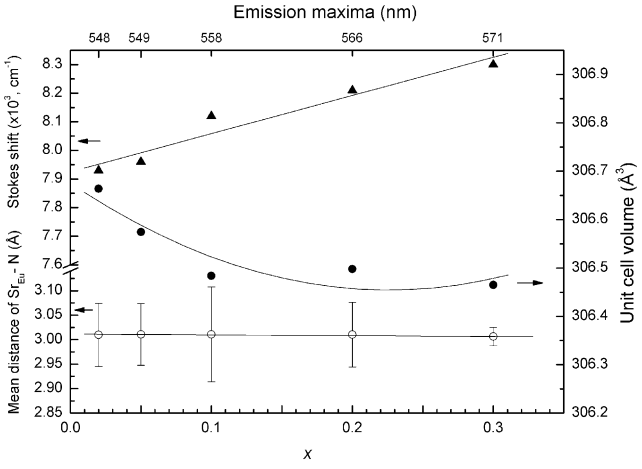

Fig. 8. Relation between x, the maxima of the emission band and the mean Sr$_{Eu}$–N distance, the unit cell volume and the Stokes shift of Sr$_{1-x}$Eu$_x$YSi$_4$N$_7$ ($0<x\leqslant 0.3$).

has a limited effect in the x range of 0 to 0.3. It can be seen (Fig. 7b) that with increasing Eu concentration the covalency slightly increases (shift of excitation band to lower energy), whereas the crystal field is hardly affected (as expected from the similar sizes Eu^{2+} and Sr^{2+}). Compared with Eu-doped BaYSi$_4$N$_7$ [16], the emission band is shifted to longer wavelength (about 30 nm) because the metal–ligand distances are smaller in SrYSi$_4$N$_7$:Eu. As a consequence, the crystal field strength and the 5*d* splitting (as deduced from the splitting of the 5*d* excitation band, Table 4) is larger. Moreover, because Ba^{2+} is larger than Sr^{2+} [25], the relaxation of the Eu^{2+} ion in the excited state possibly is larger in SrYSi$_4$N$_7$ as compared to BaYSi$_4$N$_7$, resulting in a higher Stokes shift [26–28]. Both effects maybe can explain that the emission in SrYSi$_4$N$_7$:Eu^{2+} is at lower energy (i.e. longer wavelength) than in BaYSi$_4$N$_7$:Eu^{2+}.

3.4.2. *SrYSi$_4$N$_7$:Ce^{3+}*

SrYSi$_4$N$_7$:Ce^{3+} exhibits an intense blue emission under ultraviolet excitation. A broad symmetric emission band with a maximum at about 450 nm can be observed (Fig. 9a). No distinguishable emission doublet due to transitions from the lowest 5*d* level to the $^2F_{5/2}$ and $^2F_{7/2}$ spin-orbit split 4*f* ground state level could be observed in the spectra, similar to the case of BaYSi$_4$N$_7$:Ce^{3+} [16]. However, the emission band can be fit two Gaussians centered at 435 and 473 nm, respectively (Fig. 9b), whose difference is about 1847 cm^{-1} which is in agreement with the theoretical difference between the $^2F_{5/2}$ and $^2F_{7/2}$ levels (~2000 cm^{-1} [29]). With Ce concentration increasing from 1% to 3%, no emission band shift was observed consistent with the low Ce solubility in SrYSi$_4$N$_7$.

The excitation spectrum of SrYSi$_4$N$_7$:Ce^{3+} shows three intense bands at 280, 320 and 340 nm, respectively (Fig. 9a). The bands at longer wavelengths correspond with transitions from the $^2F_{5/2}$ ground state to levels of the Ce^{3+} 5*d* configuration split by the crystal field interaction, in fair agreement with the absorption bands in the reflection spectra (Fig. 6b).

For the Ce^{3+} ion incorporated on the Y^{3+} site in *M*YSi$_4$N$_7$ (*M*=Sr, Ba), the replacement of Sr by Ba has a negligible effect on the crystal field, as deduced from the similar position of the excitation bands (Table 4).

Table 4
Luminescence data of Eu^{2+}- or Ce^{3+}-doped *M*YSi$_4$N$_7$ (*M*=Sr, Ba)

*M*YSi$_4$N$_7$	Eu^{2+}-doped			Ce^{3+}-doped		
	Excitation band (nm)	Emission band (nm)	Stokes shift (cm^{-1})	Excitation band (nm)	Emission band (nm)	Stokes shift (cm^{-1})
Sr (this work)	340, 382–386	548–570	7900–8300	280, 320, 340	450	7200
Ba (Ref. [16])	348, 385	505–537	6200–7200	285, 318, 338	415–420	4100

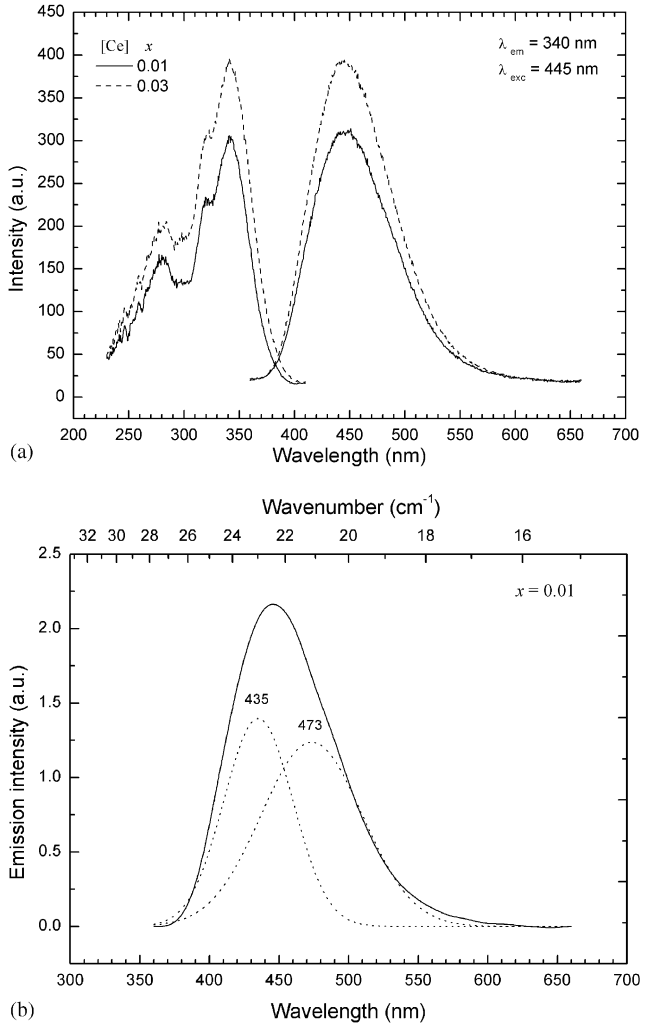

Fig. 9. (a) Excitation and emission spectra of $SrY_{1-x}Ce_xSi_4N_7$ ($0<x\leqslant 0.03$); (b) emission spectrum of $SrY_{1-x}Ce_xSi_4N_7$ ($x=0.01$) fit to two Gaussians.

Similarly to the Eu-doped case [26–28], because Ce shrinks during excitation, this shrinkage is more obstructed in an expanded host lattice, resulting in a smaller Stokes shift, and consequently the emission band is at a lower wavelength in $BaYSi_4N_7$:Ce^{3+} (415–420 nm).

4. Conclusions

$Sr_{1-x}Eu_xYSi_4N_7$ ($x=0$–1) and $SrY_{1-x}Ce_xSi_4N_7$ ($x=0$–0.05) have been synthesized by solid-state reaction method. The crystal structure of $MYSi_4N_7$ (M = Sr, Eu) isostructural with $MYbSi_4N_7$ (M = Ba, Sr, Eu), was refined from the X-ray powder diffraction pattern by the Rietveld method. $SrYSi_4N_7$ and $EuYSi_4N_7$ crystallize in the hexagonal symmetry: space group $P6_3mc$ (No. 186), $Z=2$, $a=6.0160$ (1) Å, $c=9.7894$ (1) Å, $V=306.83(3)$ Å^3; and $a=6.0123$ (1) Å, $c=9.7869$ (1) Å, $V=306.37(1)$ Å^3 for $SrYSi_4N_7$ and $EuYSi_4N_7$, respectively. The Eu^{2+} emission was found at 548–570 nm in Eu-doped $SrYSi_4N_7$ for low Eu content. Its excitation maximum is at about 390 nm, which is a favourable position for LED lighting purposes. With increasing Eu concentration the Eu^{2+} emission band shifts to longer wavelength and the emission intensity decreases. Ce^{3+}-doped $SrYSi_4N_7$ exhibits a narrow blue emission band with a maximum at about 450 nm.

References

[1] G. Petzow, M. Herrmann, Silicon nitride ceramics. In: D.M.P. Mingos (Ed.), Struct Bond (High Performance Non-Oxide Ceramics II), 2002, pp. 102–147.
[2] V.A. Izhevskiy, L.A. Genova, J.C. Bressiani, F. Aldinger, J. Eur. Ceram. Soc. 20 (2000) 2275.
[3] T. Jüstel, H. Nikol, C. Ronda, Angew. Chem. Int. Ed. 37 (1998) 3084.
[4] C. Feldmann, T. Jüstel, C.R. Ronda, P.J. Schmidt, Adv. Funct. Mater. 13 (2003) 511.
[5] J.W.H. van Krevel, Ph.D. Thesis, Eindhoven University of Technology, 2000.
[6] J.W.H. van Krevel, H.T. Hintzen, R. Metselaar, A. Meijerink, J. Alloys Compd. 268 (1998) 272.
[7] J.W.H. van Krevel, H.T. Hintzen, R. Metselaar, Mater. Res. Bull. 35 (2000) 747.
[8] J.W.H. van Krevel, J.W.T. van Rutten, H. Mandal, H.T. Hintzen, R. Metselaar, J. Solid State Chem. 165 (2002) 19.
[9] S.R. Jansen, J. Migchels, H.T. Hintzen, R. Metselaar, J. Electrochem. Soc. 146 (1999) 800.
[10] K. Uheda, H. Takizawa, T. Endo, J. Lumin. 87–89 (2000) 967.
[11] H.A. Höppe, H. Lutz, P. Morys, W. Schnick, A. Seilmeier, J. Phys. Chem. Solids 61 (2000) 2001.
[12] H. Huppertz, W. Schnick, Angew. Chem. Int. Ed. Engl. 108 (1996) 2115.
[13] H. Huppertz, W. Schnick, Z. Anorg. Allg. Chem. 623 (1997) 212.
[14] H. Huppertz, W. Schnick, Acta Crystallogr. C 53 (1997) 1751.
[15] C.M. Fang, Y.Q. Li, H.T. Hintzen, G. de With, J. Mater. Chem. 13 (2003) 1480.
[16] Y.Q. Li, G. de With, H.T. Hintzen, J. Alloys. Compd., in press.
[17] H.M. Rietveld, J. Appl. Crystallogr. 2 (1969) 65.
[18] A.C. Larson, R.B. Von Dreele, Report LAUR 86-748, 2000, Los Alamos National Laboratory, Los Alamos, NM.
[19] B.H. Toby, J. Appl. Crystallogr. 34 (2001) 210.
[20] T.C. Ekström, K.J.D. Mackenzie, M.J. Ryan, I.W.M. Brown, G. Vaughan White, J. Mater. Chem. 7 (1997) 505.
[21] S. Natansohn, A.E. Pasto, W.J. Rouke, J. Am. Ceram. Soc. 16 (1993) 2273.
[22] A.V. Virkar, T.B. Jackson, R.A. Cutler, J. Am. Ceram. Soc. 72 (1989) 2031.
[23] W. Schnick, H. Huppertz, Chem. Eur. J. 3 (1997) 679.
[24] W. Schnick, Int. J. Inorg. Mater. 3 (2001) 1267.
[25] R.D. Shannon, Acta Crystallogr. A 32 (1976) 751.
[26] G. Blasse, J. Chem. Phys. 51 (1969) 3529.
[27] G. Blasse, A. Bril, Philips Tech. Rev. 31 (1970) 314.
[28] A. Meijerink, G. Blasse, J. Lumin. 43 (1989) 287.
[29] G. Blasse, B.C. Grabmaier, Luminescent Materials, Springer, Berlin, 1994.